Catalyzing Bond-Dissociation in Graphene via Alkali-Iodide Molecules

Nilesh Vats,* Devendra S. Negi, Deobrat Singh, Wilfried Sigle,* Sabine Abb, Suman Sen, Sven Szilagyi, Hannah Ochner, Rajeev Ahuja, Klaus Kern, Stephan Rauschenbach, and Peter A. van Aken

Atomic design of a 2D-material such as graphene can be substantially influenced by etching, deliberately induced in a transmission electron microscope. It is achieved primarily by overcoming the threshold energy for defect formation by controlling the kinetic energy and current density of the fast electrons. Recent studies have demonstrated that the presence of certain species of atoms can catalyze atomic bond dissociation processes under the electron beam by reducing their threshold energy. Most of the reported catalytic atom species are single atoms, which have strong interaction with single-layer graphene (SLG). Yet, no such behavior has been reported for molecular species. This work shows by experimentally comparing the interaction of alkali and halide species separately and conjointly with SLG, that in the presence of electron irradiation, etching of SLG is drastically enhanced by the simultaneous presence of alkali and iodine atoms. Density functional theory and first principles molecular dynamics calculations reveal that due to charge-transfer phenomena the C—C bonds weaken close to the alkali-iodide species, which increases the carbon displacement cross-section. This study ascribes pronounced etching activity observed in SLG to the catalytic behavior of the alkali-iodide species in the presence of electron irradiation.

1. Introduction

The ability of modern aberration-corrected high-resolution transmission electron microscopy (AC-HRTEM) to image single atoms has greatly helped to understand single-atom catalysis (SAC) and the underlying real-time dynamic processes.[1]

SAC has played a vital role in electron-beam-assisted defect-formation reactions in 2D-materials decorated with atomic species.[2] The reported defect structures, such as, vacancies, holes, and nanoribbons, have promising applications such as molecular sieving,[3,4] confinement,[5] magnetism,[6] electrochemistry,[7] and for DNA translocation sensors.[8] SAC was shown to be triggered by transition-metal atoms and silicon,[9–11] which form covalent bonds with the underlying graphene and thus lead to some charge redistribution.[11] This weakens the C—C atom bonding in the graphene lattice and facilitates vacancy formation in the graphene lattice under high-energy electron irradiation. The dangling bonds at the vacancy site have the tendency to attract other SAC atoms due to their high reactivity compared to pristine graphene,[12] hence, resulting in additional vacancy formation ultimately leading to the formation of holes.[13–16]

Experimental studies highlight that group-I (alkali), group-III, and group-VIII (noble gas) atoms do not show SAC; instead, group-I atomic species form pure ionic bonds, and group-III atoms form partial ionic and covalent bonds with graphene.[17,18] However, the C—C bond-weakening reaction in single-layer graphene (SLG) has not been studied in case of molecular species. Of particular interest are

N. Vats, D. S. Negi, W. Sigle, S. Abb, S. Sen, S. Szilagyi, H. Ochner,
R. Ahuja, K. Kern, S. Rauschenbach, P. A. van Aken
Max Planck Institute for Solid State Research
Heisenberstr.1, 70569 Stuttgart, Germany
E-mail: N.Vats@fkf.mpg.de; W.Sigle@fkf.mpg.de

The ORCID identification number(s) for the author(s) of this article
can be found under https://doi.org/10.1002/smll.202102037.

D. Singh, R. Ahuja
Condensed Matter Theory Group
Materials Theory Division
Department of Physics and Astronomy
Uppsala University
Box 516, Uppsala 75120, Sweden
R. Ahuja
Department of Physics
Indian Institute of Technology Ropar
Rupnagar, Punjab 140001, India
K. Kern
Institut de Physique de la Matière Condensée
École Polytechnique Fédérale de Lausanne
Lausanne CH-1015, Switzerland
S. Rauschenbach
Department of Chemistry
University of Oxford
12, Mansfield Road, Oxford OX1 3TA, UK

**ADVANCED
SCIENCE NEWS**
www.advancedsciencenews.com

**NANO · MICRO
small**
www.small-journal.com

group-I and group-VII elements, as single adatoms of these groups show only weak interaction with SLG, whereas the ionic interaction between such species is very strong. Besides, group-I and group-VII elements deposited on graphene and graphite have been extensively investigated individually using TEM toward their application in the field of graphite intercalation compounds. Their adsorbed atomic species exhibit ionic characteristics by exchanging electrons with the host (graphite/graphene) material.[19–21]

In this work we show, both experimentally and theoretically, that the presence of alkali-iodide molecular species enhances the rate of etching in SLG under electron irradiation. For this, we employ the electrospray ion-beam deposition (ES-IBD)[22–25] technique to deposit chemically selected alkali-metal (AM), iodine (I), and alkali-iodide (AI) ions on SLG. We perform AC-HRTEM time-dependent atomic-scale characterization of the etching process and the morphology of the graphene. Application of both techniques thus offers the advantage of highly controlled sample synthesis and atom-by-atom characterization in real time. Moreover, using density functional theory (DFT), the electronic interaction between AM, I, and AI with SLG, the charge transfer, and the static binding energy are elucidated. Using first-principles molecular dynamics (FP-MD), we evaluate the dynamic threshold displacement of carbon atoms at 80 kV.

2. Results and Discussions

Alkali (Cs^+, Rb^+), iodine (I^-), and alkali iodide [$(AI)_nA^+$] (here A= Na, K, Rb, and Cs) ionic species were deposited on graphene after mass-selection in ES-IBD. The landing energy of the deposited ionic cluster species was set to 200 eV per charge and the final coverage of the alkali and alkali-iodide ionic species recorded on the surface of TEM grids varied between ≈450 and 500 pAh. For iodine, the total coverage after the completion of deposition was 100 pAh. The mass spectra of all deposited ionic-cluster species are shown in Figures S1 and S2, Supporting Information.

The alkali iodides form 3D-nanoparticles on the graphene surface (Figure S3, Supporting Information) quickly disintegrate into adatoms, small clusters, and atom pairs upon electron irradiation (refer Video S1, Supporting Information).[26] This leads to the formation of a high density of atomic species on the surface of graphene. In Figure S4a–f, Supporting Information, the structure of 3D-nanoparticles of alkali-iodides are analyzed using their 2D-FFT along [001] viewing direction. The measurement suggests that their structure corresponds to their bulk counterparts, that is, CsCl-bcc-type for CsI and NaCl-fcc-type for RbI and NaI nanocrystal. In contrast, Cs, Rb, and I do not form such 3D-nanoparticles but are dispersed on the graphene surface as adatoms.

After prolonged electron irradiation (≈30 s) at an electron kinetic energy of 80 keV, holes form in the graphene near the adsorbed alkali-iodide clusters (**Figure 1**a–d and Video S2, Supporting Information). Due to the high reactivity of the dangling carbon bonds present at the SLG holes, some alkali and iodine atomic species decorate the edges of the holes, as shown in the insets enclosed in black boxes of Figure 1a–d. However,

the majority of alkali (Cs and Rb) and iodine (I) atom species adhere to energetically favorable sites such as hydrocarbon impurities and steps of the polycrystalline graphitic surface (**Figure 2**a–f). Individual Cs, Rb, and I atoms on the SLG surface can be readily identified due to their high contrast compared to the carbon atoms. Moreover, unlike the AI-dimer case, the presence of individual AM and I adatoms on the SLG does not instigate formation of holes under continuous electron irradiation and the lattice of SLG remains intact (refer Videos S3 and S4, Supporting Information).

2.1. Rate of Etching

During extended electron irradiation, the size of the graphene holes in the presence of alkali-iodide species increases (**Figure 3**a–t). The contours of the holes formed in graphene sheets are not exactly circular, but irregular, and therefore the quantification of the SLG-hole growth is performed by measuring the hole perimeter as a function of time. In Figure 3a–d, we show the time dependence of the hole growth in SLG at an electron current density of 1.16×10^6 e nm^{-2} s^{-1}. The edges of the holes shown in Figure 3a–d are decorated with Cs and I ions. These ions migrate along the periphery of the hole under electron-beam irradiation. The perimeter of the hole increases from 3.5 to 9.3 nm after 129 s and the rate of growth of the perimeter is 0.04 nm s^{-1} (or 2.4 nm min^{-1}). Here, the hole growth rate is evaluated from the slopes of the linear fit to the plotted data points representing increase in the hole perimeter as a function of time. Furthermore, the rate of etching was computed for four different holes for every alkali-iodides (NaI, KI, RbI, and CsI) and are tabulated in Table S1, Supporting Information. The average values of the different slopes for all samples are plotted in **Figure 4**. In general, during HRTEM imaging, the reservoir of ionic species along the hole edge does not disappear as the hole expands and their participation is uninterrupted during the etching process, until it leads to the complete destruction of the graphene membrane in the course of time.

Etching is not only observed in SLG, but also in BLG in the presence of Cs and I ions. It was found that initially a hole is formed in only one of the two layers, and only in a later stage the second layer is etched as well. Figure 3e–h shows the expansion of a hole in bilayer graphene from 7.2 to 13.2 nm during a period of 564 s. The edge of the hole is marked by a dashed yellow line. The Moiré pattern outside the hole is a signature of BLG with 4° twist between two SLG sheets. In the interior of the yellow dashed line, we observe the lattice of SLG. This shows selective etching of one layer. Similar to the case of SLG, cesium (Cs) and iodine (I) ions are attached to the edge of the hole. After 244 s (Figure 3f), the perimeter of the hole has increased to 8.2 nm and still only one layer is affected by the etching process. After 421 s (Figure 3g) the perimeter of the hole has increased to 12 nm and, in the top left edge of the hole, one can see etching has begun in the second carbon layer, marked by a dashed red line. Interestingly, we observe that the rate of hole growth in BLG is approximately 3 times slower compared to SLG (see **Table 1**). CsI etches BLG much slower than SLG. This can be understood from the stronger bonding of C atoms in BLG because of the presence of the second graphene layer.
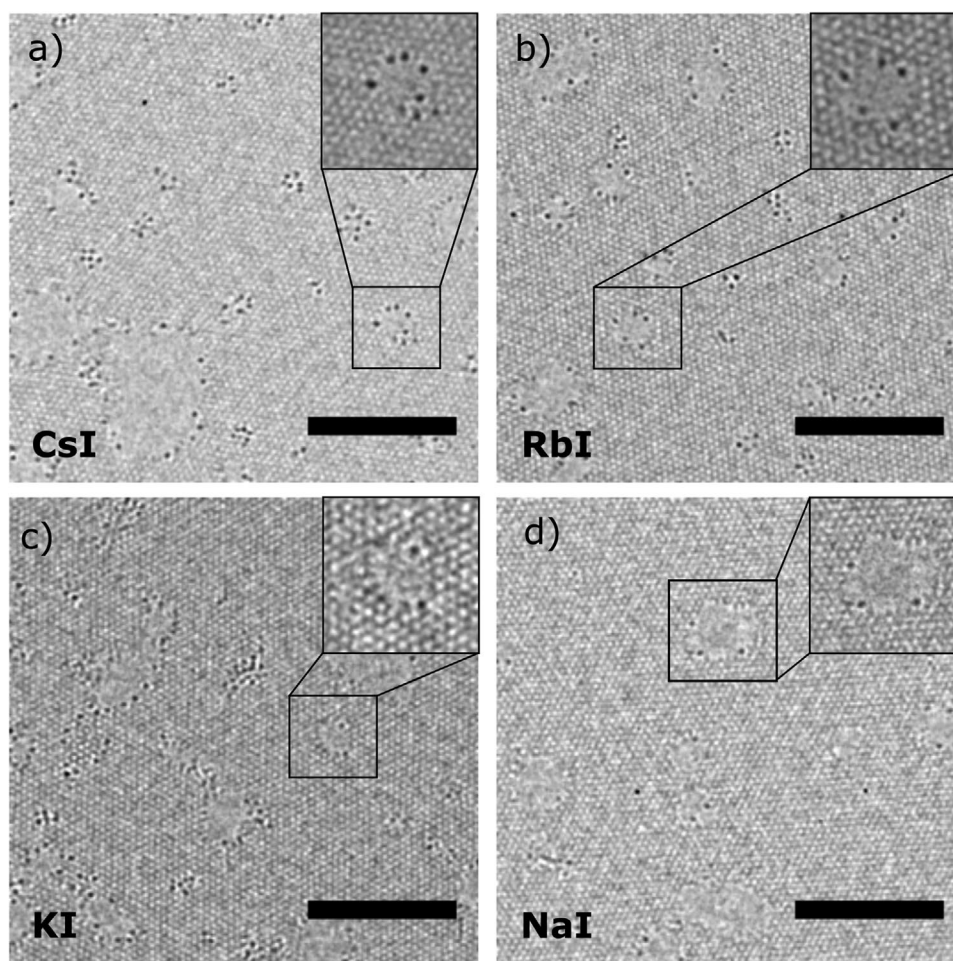
Figure 1. HRTEM images of single-layer graphene with alkali-iodide adatoms. a) Cesium iodide, b) rubidium iodide, c) potassium iodide, and d) sodium iodide clusters on SLG. Insets in (a–d) show graphene pores decorated with alkali-iodide clusters formed under electron irradiation at 80 kV. HRTEM images were smoothened by applying Gaussian-blur of sigma radius 1.0, using ImageJ software. The scale bar corresponds to 5 nm.

In our attempt to ascertain the influence of cesium and iodine ions in the etching procedure, we analyzed the rate of growth of holes in pristine SLG under electron irradiation in the TEM at 80 kV, in the absence of Cs and I ions. Defect-free, pristine SLG, is robust and highly stable under 80 kV acceleration voltage in TEM. The maximum energy transferred to a carbon atom in graphene via elastic scattering is 15.8 eV[15] and this is smaller than the energy required to produce knock-on damage in the graphene lattice, which is 21.38 eV. Therefore, we started with two pre-existing holes and observed their growth under electron irradiation (Figure 3i–l). The holes grow as the threshold for atom displacement from the edge of the hole is well below 15.8 eV. The rate of hole expansion was calculated to be 0.83 nm min^{-1}. This value is approximately three times smaller than the average etching rate for SLG pores in the presence of Cs and I ions. Furthermore, the rate of graphene pore expansion was studied in SLG, when Cs (Figure 3m–p) and I atoms (Figure 3q–t) were individually present at the pre-existing SLG pore edges. In this case, we found a lower density of ions along the hole edges as compared to the situation, where Cs and I ions are present simultaneously. The calculated rate of growth of the SLG hole perimeter is 0.52 nm min^{-1} for Cs and

0.48 nm min^{-1} for I (Table 1). Surprisingly, this rate of hole growth is smaller than that of SLG (≈0.8 nm min^{-1}) without any ad-atom species implying that their presence hinders the rate of hole growth in similar irradiation condition at 80 kV. A possible reason for this may be the presence of graphitized hydrocarbon impurities (see Figure 3m–t) at the edges of the holes, which may impede hole growth.

These results imply that the individual Cs and I atoms interact weakly with the SLG hole edge in comparison to CsI. Therefore, the mechanism of hole expansion is hardly affected by the presence of only Cs or I atoms. The rate of etching values evaluated for other AI ionic species (KI, RbI, and NaI) are tabulated in Table S1, Supporting Information. The values of NaI and RbI are lower than the CsI results, but approximately twice the values for the pure I or Cs adsorption. This is a clear evidence that the simultaneous presence of alkali and iodide ionic species stabilizes their occupancy at the SLG-hole edges and consequently dictate higher rate of SLG-hole growth. Moreover, the rate of hole expansion in pristine SLG is similar to the growth rate calculated for pores in BLG decorated with Cs or I ions. These results demonstrate that AI atomic species act as reliable catalyst agents for etching
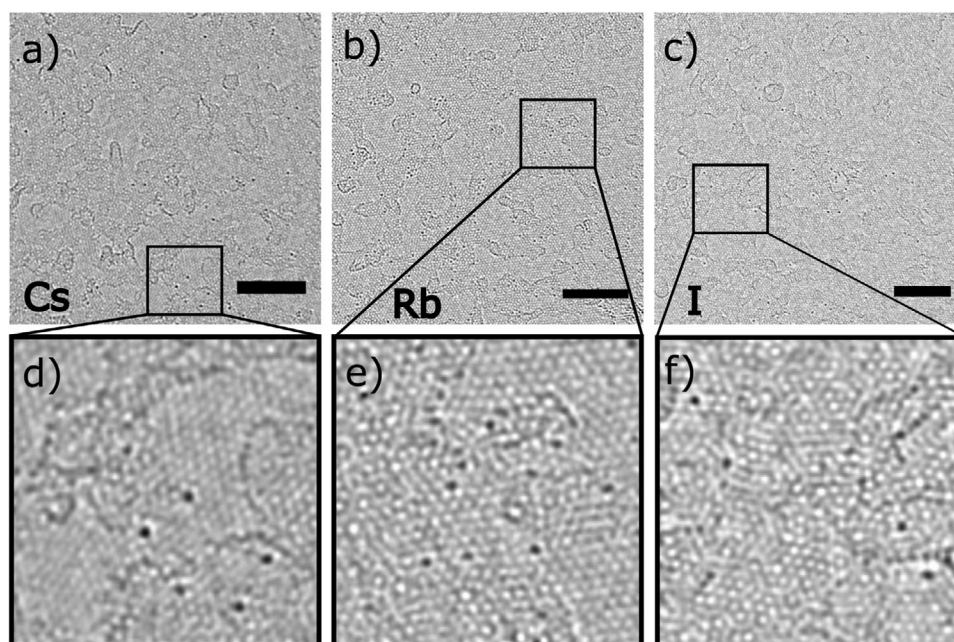
Figure 2. HRTEM image of single-layer graphene with adatoms. a) Cesium, b) rubidium, and c) iodine adatoms. d–f) Enlarged view of the selected area enclosed by the black box in (a–c) showing adatoms adhering specifically to hydrocarbon impurities present on the SLG surface. d–f) Enlarged HRTEM images were smoothened by applying Gaussian-blur of sigma radius 1.5, using ImageJ software. The scale bar corresponds to 5 nm.

SLG under electron-beam irradiation. They are not consumed during the etching process, as it is the case for lighter atoms, like Si, which experience considerable momentum transfer from the fast electrons at 80 kV.

2.2. Interaction of Alkali Metal and Iodine Adatoms with Single-Layer Graphene

Interaction of individual AM, I, and AI species with SLG is key to understanding the etching process in SLG in the presences of the AI species under prolonged electron irradiation. Therefore, we performed first-principles DFT calculations (refer to Section 4), which revealed the nature of these interactions. At first, we benchmarked our calculations by comparison with already published data involving AM and I adatoms on SLG.[17,18,27] The results obtained from our DFT calculations were in agreement with these calculations and we therefore, in the next step, performed calculations involving AI dimers.

In **Figure 5**, the nature of the interaction of AM and I adatoms with SLG is described. The energetically optimized structure of AM and I (Na, K, Rb, Cs, and I) adatoms along [001] and [100] viewing directions is shown in Figure 5a–j. Because the electron density at the "H" site is lower as compared to that at the "T" and "B" sites, the "H" site is the energetically stable position of an adatom.[17] The height of adsorption (d) above the graphene plane for AMs gradually increases from Na (0.27 nm) to Cs (0.30 nm), and for I it is 0.37 nm (Table S2, Supporting Information). The nature of interaction of AM and I adatoms with SLG was evaluated by computing the charge-density difference $\Delta\rho(\mathbf{r})$ before and after adsorption (Figure 5k–n). The charge density difference is calculated using the following equation:

$$\Delta\rho(\mathbf{r}) = \rho(\mathbf{r})_{aG} - \rho(\mathbf{r})_a - \rho(\mathbf{r})_G \qquad (1)$$

where $\rho(\mathbf{r})_{aG}$ is the total charge density of the alkali-metal adatom and SLG, $\rho(\mathbf{r})_a$ is the charge density of the isolated alkali-metal atom and $\rho(\mathbf{r})_G$ is the charge density of the isolated SLG. In Figure 5k–n, charge accumulation and depletion are denoted by yellow and cyan colors, which suggests that interaction leads to depletion of charge from the AM adatoms and accumulation of charge above the SLG surface. The accumulated charge is dispersed all over the SLG surface. Figure 5o shows that in case of I adatoms the charge-density difference is inverted as compared to the AM adatoms. Hence, AM adatoms donate (s) electrons from their outermost electronic shell to SLG and therefore become positively charged, whereas I adatoms become negatively charged after receiving (p_z) electrons from SLG.

In addition, the charge separation is clearly observed in Figure 5p–t, where the charge-density difference is plotted along the [100] viewing direction. Obviously, only exchange of charge has taken place between substrate and adatoms leading to a purely ionic interaction. The values of charge transfer are shown in Table S2, Supporting Information. The electron-density distribution within the graphene plane (Figure 5u–y) looks very similar for all adatoms, indicating that the C–C bonding within the SLG is hardly affected by the adatom adsorption.

2.3. Interaction of Alkali-Iodide Dimers with Single-Layer Graphene

In **Figure 6**, the interaction of AI dimers (NaI, KI, RbI, and CsI) with SLG is shown. Energetically optimized structural configurations along [001] and [100] viewing direction are shown in Figure 6a–h. The height of adsorption of AI-dimer atoms above
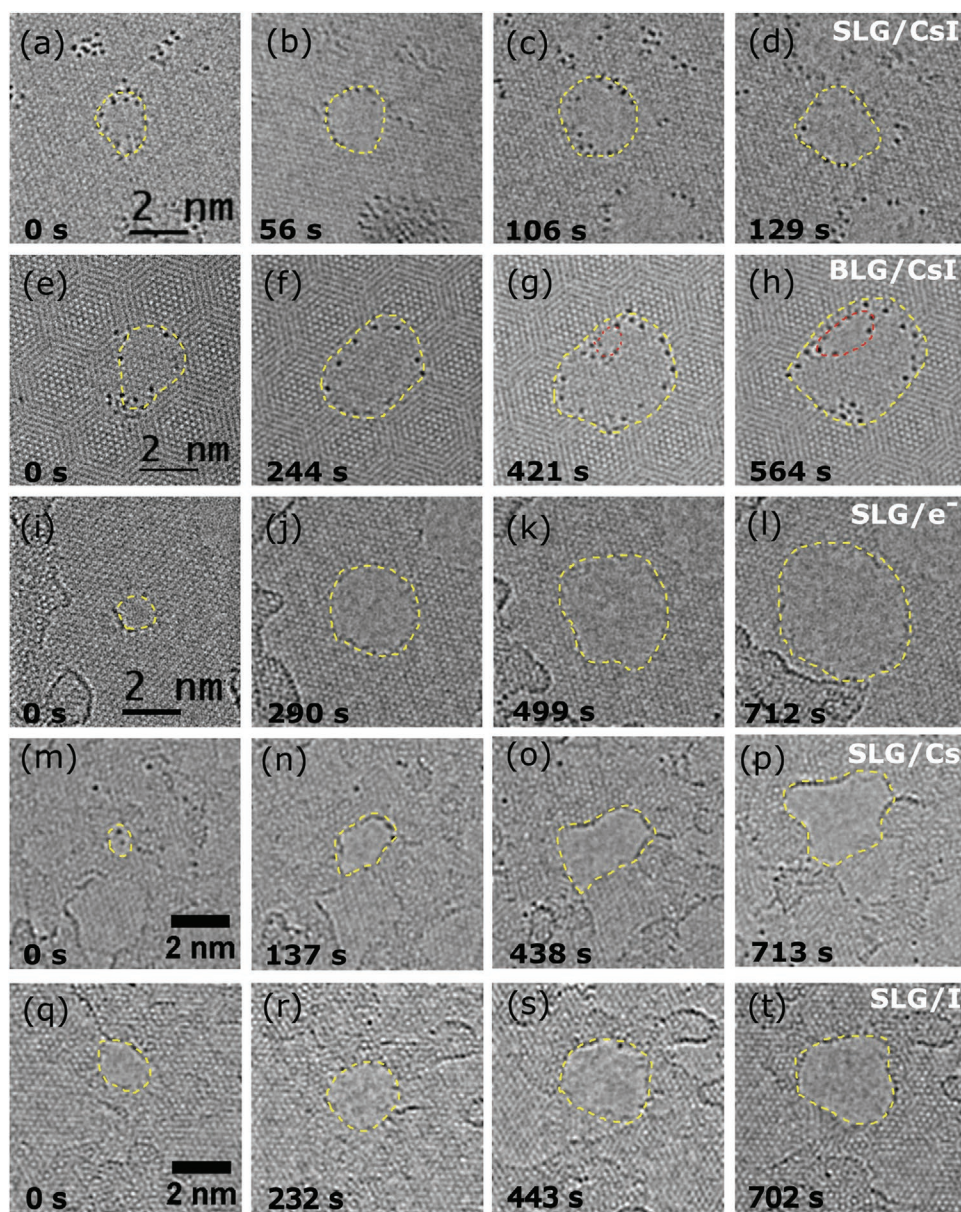
Figure 3. Time-sequence of hole expansion during 80 kV electron irradiation in SLG and BLG with CsI, Cs, I and with only the electron beam. Increase in the perimeter of a hole in a–d) SLG and e–h) BLG with CsI. i–l) Enlargement of a SLG pore by electron radiation only. Increase in the perimeter of a hole in SLG with m–p) Cs atoms and q–t) I atoms. HRTEM images were smoothened by applying Gaussian-blur of sigma radius 1.0, using ImageJ software.

the SLG plane and the respective adsorption energies are presented in Table S3, Supporting Information. Calculated bond lengths of the AI dimers (i.e., NaI 2.77 Å, KI 3.11 Å, RbI 3.25 Å, and CsI 3.41 Å) from the DFT optimized structural configuration are in agreement with literature values.[25] Interestingly, the dimers cause buckling of the SLG lattice. Only in case of CsI, this buckling is almost negligible (Figure 6h). The buckling leads to both in-plane and out-of-plane distortions and thus to strain in the SLG lattice. The minimum and the maximum in-plane distortions are 0.01 Å (RbI) and 0.02 Å (NaI), which corresponds to positive strain of 0.7% and 1.4%, respectively. The in-plane strain produced in the SLG lattice for NaI, KI, and RbI dimers is shown in Figure S5, Supporting Information. In

addition, the calculated amplitudes for the out-of-plane distortions in SLG are −0.48 Å, −0.52 Å, and −0.51 Å for the NaI, KI, and RbI dimers (Figure S6, Supporting Information).

The 3D charge density along the [001] viewing direction is plotted in Figure 6i–l. The charges are locally confined to the adsorption site of the AI dimers on the SLG lattice. This is in stark contrast to what was observed for the AM and I adatom case, where the accumulated and depleted charges were dispersed homogeneously over the SLG (Figure 5k–o). The charge-density maps along the [100] viewing direction shown in Figure 6m–p demonstrate the separation of the charge at the interface between SLG and AI dimers. The dimer exhibits a charge accumulation at the electronegative I atom and a
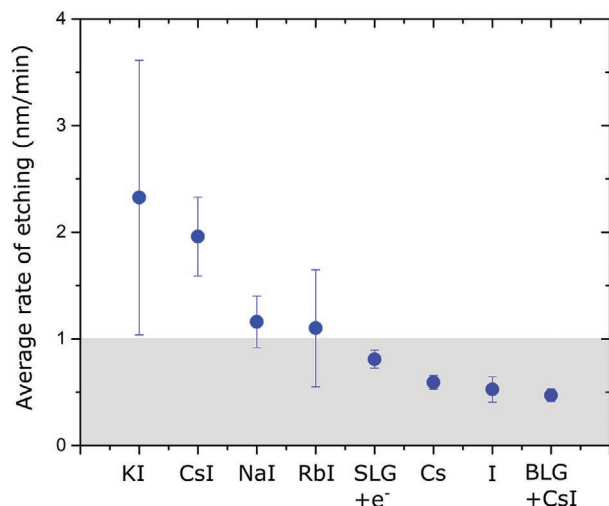
Figure 4. Plot comparing the average rate of etching values calculated for CsI, RbI, KI, NaI, I, Cs adsorbed on SLG and CsI on BLG. Also shown is the etching rate for pristine SLG under electron irradiation.

depletion of charge at the electropositive AM atom. Moreover, a discernable separation of the density of electronic charge in the SLG at the site of the dimer adsorption suggests a non-covalent interaction between the AI dimer and SLG. Besides, the interaction between the AI dimer and SLG leads to a depletion of the C−C bonding electron density in the SLG lattice (Figure 6q–t). Unlike the adsorption of individual alkali/iodine atom on SLG (Figure 5p–t), quadrupole charges are generated due to alkali-iodide dimer adsorption (see Figure 6m–p). The presence of additional pair of positive and negative charges results in enhanced interaction between SLG and the alkali-iodide dimer molecule. This forbids the charges from delocalizing on the SLG surface, and the charges generated after adsorption are all confined to the site of adsorption. As the charge transfer w.r.t, SLG is localized, the charge depletion in SLG is also localized and hence we observe charge redistribution between C−C bonds in SLG (refer Figure 6q–s). Which in turn reduce the bond strength between C−C atoms and can alter their overall binding energy at the site of (AI) adsorption. The additional charge depleted from SLG at the site of adsorption is compensated by the buckling of the SLG, which helps in minimizing the total energy of the system (refer Figure 6a–c).

Notably, the depletion of electrons in SLG takes place at the AI dimer adsorption site (Figure 6q–s), with the exception of CsI, where reduction in electron density is not localized at the site of adsorption, but it is rather reduced homogenously from the SLG surface as observed in (Figure 6t) due to overall reduction in (red) color intensity. This behavior can be attributed to its increased height of adsorption compared to other AI dimers (refer Table S3, Supporting Information), that in turn

minimizes its interaction strength w.r.t SLG and therefore, leading to no noticeable buckling in the underlying SLG sheet.

The density-of-states (DOS) analysis shown in Figures S7 and S8, Supporting Information, provides additional insight into the electronic properties after adsorption on SLG. The DOS analysis shows that the interaction of AM and I adatoms neither alters nor hybridizes with the energy states of SLG upon adsorption. The DOS of the adsorbed atom contains only localized states of free AM and I atoms, which implies the ionic nature of the electronic interaction. The same is true for the AI dimer case, where the electronic interaction of the AI dimer and SLG does not alter or hybridize with the energy states of SLG, implying pure ionic interaction. However, due to the electronic interaction between I and AM atoms in an AI dimer, the DOS energy distribution shows a hybridization of orbitals between AM-s state and I-p state.

2.4. Calculation of Binding Energy

A direct consequence of the charge depletion between carbon atoms is a reduction in their binding energy. In order to verify this, two carbon atoms were selected in the vicinity of either the AI dimer, the AM adatom, or the I adatom adsorption sites, and their corresponding binding energies (E_b) were calculated. Carbon atoms at different distances from the adatom/dimer were selected for the calculation, which are denoted as "near" and "far" (Figure S9, Supporting Information). The binding energy values for the two cases were computed using the following equation:

$$E_b = E_v + E_s - E_T \qquad (2)$$

where E_b is the binding energy, E_v the total energy of the combined system with a C-atom vacancy at the selected site, E_s the total energy of a single carbon atom in SLG, and E_T the total energy of the combined system. The calculated values for both dimer and adatom cases are given in **Table 2**. The calculated E_b for the AI dimers is approximately half the value for the AM and I adatoms. For instance, the E_b value calculated for the nearest carbon atom in SLG is 13.43 eV underneath a Na adatom, whereas it is 6.46 eV underneath the NaI dimer, suggesting that the C−C bond has weakened by approximately a factor of two near the adsorption site of the NaI dimer as compared to that of the Na adatom. This trend is common for both the "near" and "far" carbon atoms. Moreover, the value of E_b calculated in pristine SLG is 18.26 eV, which is higher than those calculated for the AI dimer, AM, and I adatom cases. The average reduction in the values of E_b upon AM adsorption is ≈3.5 eV whereas it is 11.4 eV for the AI dimer adsorption.

The reduction in E_b undeniably facilitates bond breaking, for example, during electron irradiation. The fast electrons in

Table 1. Comparison of average graphene etching rates, calculated from multiple holes in each case of CsI, RbI, KI, NaI, I, and Cs adsorption on SLG; In addition, the average etching rate of BLG is shown for CsI adsorption. The electron acceleration voltage was 80 kV.

Samples	SLG+CsI	SLG+RbI	SLG+KI	SLG+NaI	SLG+I	SLG+Cs	SLG+e⁻	BLG+CsI
Rate of etching [nm min⁻¹]	1.86 ± 0.34	1.10 ± 0.6	2.33 ± 1.29	1.15 ± 0.24	0.48 ± 0.06	0.52 ± 0.12	0.83 ± 0.08	0.6 ± 0.06

ADVANCED
SCIENCE NEWS
www.advancedsciencenews.com

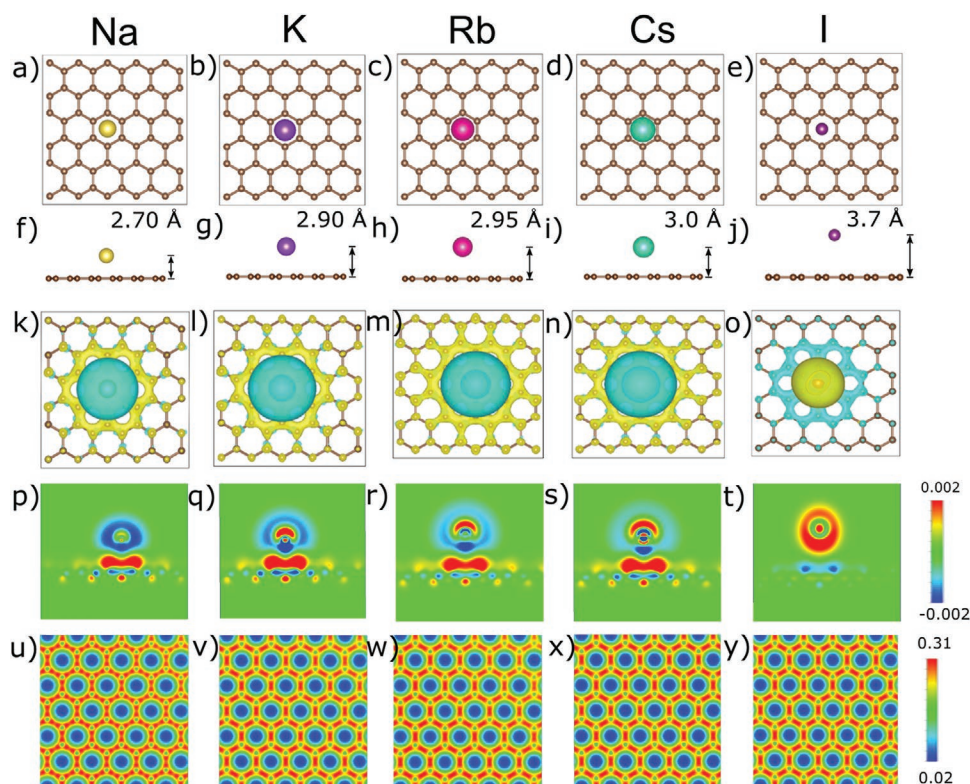NANO · MICRO
small
www.small-journal.com

Figure 5. Interaction of alkali metal and iodine adatoms with SLG. Energetically optimized structural model of Na, K, Rb, Cs, and I ad-atom on SLG viewed a–e) along the [001]-direction and f–j) along the [100]-direction. k–o) 3D charge-density difference plot along the [001] viewing direction and p–t) charge-density plot of the cross-section through alkali and iodine adatoms perpendicular to SLG. u–y) 2D-charge density distribution in the SLG plane underneath the alkali ad-atom. The unit used for the electron density is (e Å^{-3}).

the TEM can break bonds, whenever the energy imparted to the target atom exceeds its ejection threshold value. To quantify this process, FP-MD simulations were performed (see Section 4) and displacement-threshold energies (T_d) of carbon atoms in SLG were determined in the presence of AI dimers, AM, and I adatoms at an electron kinetic energy of 80 keV (Figures S10 and S11, Supporting Information, and Table 2). The T_d value calculated for the carbon atom in pristine SLG was found to be 21.38 eV, which is in good agreement with the previously reported value of 21.37 eV that considers van der Waals corrections.[29] In comparison to pristine SLG, T_d values were found to be reduced by (2.33–4.34 eV) for the AI dimer, by (1.81–1.94 eV) for the AM, and by 0.74 eV for the (I) adatom case. As expected from the change in E_b, this shows that the carbon atoms situated near the AI dimer adsorption site require less energy to be completely displaced from the SLG lattice compared to carbon atoms close to the AM and I adatoms.

Based on calculated T_d values for carbon atoms, their corresponding theoretical cross-sections for displacement, σ_d, were calculated using the modified McKinley and Feshbach equation,[13,26] in which the Gaussian distribution of atomic vibrations are included (see Section 4). The cross-sections in pristine SLG are shown for comparison. The total cross-sections for carbon atoms situated near and far from the AI dimer, AM and (I) adatom adsorption sites, are plotted in Figure S12a,b, Supporting Information for different acceleration voltages, and the corresponding values are given in Table 2. At 80 kV, the σ_d value for a carbon atom in pristine SLG is close to zero (i.e.,

≈10^{-5} barn), whereas for carbon atoms near the adsorption sites of AI dimers the cross-section σ_d increases by an amount of 0.01 to 0.7 barn from CsI to NaI (see Table 2). The non-zero σ_d values in the AI dimer case at 80 kV (Figure S12a, Supporting Information) implies that non-destructive imaging of SLG at this particular imaging condition is not possible and the SLG will suffer substantial knock-on damage. This will lead to significant damage in the SLG after prolonged electron irradiation (i.e., 10 to 100 s), which is indeed observed in our experiments (see Figure 2a–d). In contrast, the value of σ_d for the AM and I adatom case remains practically zero (i.e., ≈10^{-4}) at 80 kV (Figure S12b, Supporting Information) and therefore, no significant alteration in the SLG lattice is observed in our HRTEM experimental images shown in Figure 1a–d. Besides, the carbon atom situated "near" the adsorption site shows more susceptibility to electron-induced damage compared to the one situated at the "far" position (Table 2 and Figure S12a,b, Supporting Information).

3. Conclusion

In summary, we studied the stability of SLG in the presence of AI dimers and AM or I atoms under the influence of electron irradiation. We combined experimental results obtained in the TEM with a thorough theoretical analysis and showed that adsorption of AI dimers on SLG leads to a weakening of C−C bonds and consequently reduces the threshold energy
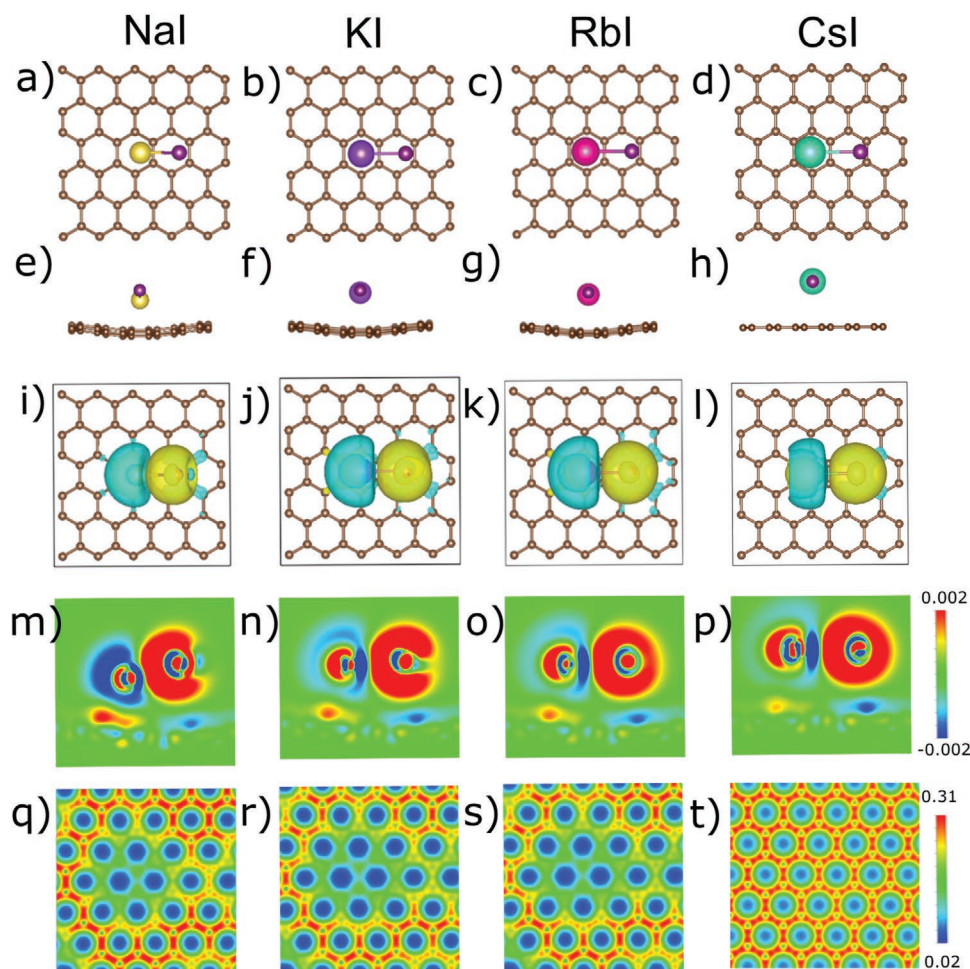
Figure 6. Interaction of alkali-iodide dimers with SLG. Energetically optimized structural models of NaI, KI, RbI, and CsI dimers on SLG viewed a–d) along the [001]-direction and e–h) along the [100]-direction. i–l) 2D charge-density-difference plots along the [001] viewing direction and m–p) 2D-charge density plots of the cross-section through alkali-iodide dimers perpendicular to the SLG. q–t) Variation in 2D-charge-density distributions in the SLG plane underneath the alkali-iodide dimers. The unit used for electron density is (e Å^{-3}).

Table 2. Values of binding energy E_b, dynamic threshold T_d and cross-section for carbon atom displacement σ_d calculated for the AM, I, and AI dimer case.

Case	E_b [eV]		T_d [eV]		σ_d [barn]	
	Near	Far	Near	Far	Near	Far
AM and I adatoms						
Na	13.43	14.20	19.48	20.38	0.0039	≈10^{-4}
K	14.79	15.24	19.53	20.43	0.0037	≈10^{-4}
Rb	15.00	15.41	19.54	20.35	0.0037	≈10^{-4}
Cs	15.58	15.96	19.56	20.39	0.0037	≈10^{-4}
I	16.99	18.11	20.67	21.20	0.0001	≈10^{-4}
SLG	18.26		21.38	21.38	≈10^{-5}	
AI-dimers						
NaI	6.46	6.84	17.03	20.61	0.7081	≈10^{-4}
KI	6.71	6.72	17.67	20.96	0.2209	≈10^{-4}
RbI	6.74	7.18	18.82	20.92	0.0207	≈10^{-4}
CsI	7.53	7.73	19.05	20.92	0.0100	≈10^{-4}

for carbon-atom displacement. Consequently, SLG damage is pronounced for an electron kinetic energy of 80 keV, whereas under these conditions no damage is observed in pristine SLG. Thus, AI species play a central role in the etching process by catalyzing the bond breaking reaction in SLG. Our assertion is that it is the pairing of two atomic species of opposite ionic character, which dramatically reduces carbon bonding in SLG. This effect is not observed, if only AM or I atom species are deposited on SLG. Hence, the observed process can be termed as "atom-pair catalysis" to highlight the cumulative phenomenon of the hetero-nuclear atomic species. We note that this is different from "di-atom catalysis," where two atoms of the same species (i.e., a platinum-dimer) participate in the hydrolysis of ammonia borane.[30]

4. Experimental Section

Graphene Transfer onto a Transmission Electron Microscopy Grid: Polymethylmethacrylate (PMMA)-free graphene suspended on a TEM grid was formed similar to the method described by Longchamp

ADVANCED
SCIENCE NEWS

www.advancedsciencenews.com

NANO · MICRO
small
www.small-journal.com

et al.[31] Commercially available CVD-grown graphene on a copper foil (Graphenea S.A.) was used throughout our experiments. As the first step, a 150 nm thick PMMA film was spin-coated onto the graphene on Cu. The copper film was then etched by floating the PMMA-SLG-Cu assembly in an etching solution (8 g of ammonium persulfate in 100 mL of deionized water). After Cu etching, the PMMA–graphene stack was transferred to a de-ionized water bath for removing the APS solution residue. Subsequently, the stack was transferred onto a platinum-coated (thickness ≈ 15 nm) perforated silicon-nitride TEM grid. In order to remove the PMMA, the TEM grid was annealed in ambient air at 300 °C for 30 min, whereupon the thin platinum layer catalyzed the oxidation of the PMMA.

Electrospray Ion-Beam Deposition: The ES-IBD setup[24] was used to generate intact positive gas-phase ions of $((AI)_nA^+)$ (where A = Na, K, Rb, and Cs), Cs^+, Rb^+ and negative gas-phase ions of I. The generated gas-phase ions were deposited on the graphene substrate in vacuum. The analyte solution (≈10^{-4} mol L^{-1} in H_2O) was pumped through an emitter capillary held at a high electric potential difference of 2–3 kV with respect to the vacuum-transfer capillary. A fine mist of charged droplets containing the analyte molecule was emitted. The ions were generated under ambient conditions through an iterative coulombic fission, while the solvent evaporated. The ions pass through four differential pumping stages to the deposition target held at 10^{-6} mbar. On their way, radio frequency (rf)-ion optics collimated the beam with an ion funnel in the first and an rf-only quadrupole in the second stage. A further rf-quadrupole was used as a mass filter to generate a chemically pure beam of the desired ion, which was confirmed by an integrated time-of-flight mass spectrometer, before the beam was used for deposition. The salient feature of ES-IBD was that the collision energy can be controlled and thereby the interaction of the molecule with the surface. Most importantly, molecules can be soft-landed destruction-free onto a surface or collided at high energies to deliberately cause fragmentation or surface defects. Further, online current monitoring allowed for precise knowledge of the deposited charge and thus for the control of the deposition coverage. Further details of the ES-IBID technique were described elsewhere.[23,24]

High-Resolution Transmission Electron Microscopy: AC-HRTEM was performed using a JEOL ARM200F TEM equipped with a cold field-emission gun and a post-specimen spherical aberration corrector (C_s) operated at an acceleration voltage of 80 kV. The spherical aberration was tuned to ≈1 µm, and the imaging was done at under-focus conditions, leading to atoms appearing dark.

Density Functional Theory: The electronic structure calculation was based on the DFT, as implemented in the Quantum Espresso package.[32–34] The core electrons and ion-electron interactions were treated with pseudo-potentials. The generalized gradient approximation in the form of Perdew–Burke–Ernzerhof functional was accounted for treating the exchange correlation energy. The electronic wave functions with a plane wave basis were truncated at an energy cutoff of 40 Ry. Similarly, the charge density was represented in the basis set with an energy cut-off of 400 Ry. The structural relaxation process was carried out with a force threshold of 1×10^{-1} Ry/Bohr. Self-consistent field (SCF) calculations were carried out with an energy-error tolerance of 1×10^{-8} Ry. The Monkhorst–Pack (MP) method[35] with ($10 \times 10 \times 1$) k-points mesh were selected for the SCF calculations. The van der Waals corrections were incorporated with the DFT-D3 scheme. The interaction of alkali-metal adatoms with SLG was calculated by simulating a ($6 \times 6 \times 1$) unit of graphene with 10 Å vacuum space both above and below the unit cell. The optimum lateral (H, T, B) and vertical (z) positions were considered from the previous calculations. However, the vertical (z) distance of alkali-iodide (AI) dimer was obtained from a structural optimization. The electronic structure and charge-density-difference plot had been derived using the VESTA program.[33]

First Principles Molecular Dynamics (FP-MD): First-principles molecular dynamics (MD) simulations with a micro-canonical (NVE) ensemble were implemented in the Vienna ab-initio simulation package

code[37,38] with an energy cut-off of 500 eV and a time step of 0.1 fs for estimating the displacement threshold energy. The velocity of the atoms was initialized by a Maxwell–Boltzmann distribution at 300 K. The projector augmented wave potentials were used to describe the core electrons, and the local density approximation functional was used for exchange and correlation. The atomic structures were fully optimized without symmetric restrictions and a 1×10^{-3} eV energy convergence criterion. A ($5 \times 5 \times 1$) Monkhorst-Pack k-point grid was used to sample the Brillouin zone.[35] A vacuum layer of 20 Å was used to remove the physical interactions between periodic images. To obtain the threshold energy, the initial momentum of a certain C atom was tuned, until it was just barely removed from the system, which corresponded to the minimum energy that was required to remove the C atom from the system.

Total Cross-Section of Atomic Displacement with Vibrations: The total cross-section of carbon atom displacement with atomic vibration $\sigma_d(T,E_e)$ was calculated by using following integral equation:[29]

$$\sigma(T,E_e) = \int_{E_{max}(\nu,E_e) \geq T_d} P(\nu,T)\sigma(E_{max}(\nu,E_e))\, d\nu \tag{3}$$

This equation was the result of the numerical integration of the modified McKinley and Feshbach equation for cross-sections as a function of maximum transferred energy to the nucleus $\sigma(E_{max}(\nu,E_e))$ multiplied by the probability distribution of the velocity of the target atoms in the direction parallel to the incoming electron beam ($P(\nu, T)$). Moreover, the maximum energy that can be transferred to a nucleus of mass M, moving with a velocity (ν), by an electron of mass m_e with energy E_e (where, $E_e = eU$ and U is the acceleration voltage) is given by the function $E_{max}(\nu, E_e)$.

Further data on ESI time-of-flight mass spectrums of the deposited species, TEM images of the 3D-nanoparticles of AI species, Tables showing list of values obtained from DFT calculations, strain analysis, DOS and FP-MD plots (PDF). Videos (.AVI) SI-video-1, 2, 3 and 4 display (using times-series HRTEM images) decomposition of RbI nanocrystal, etching behavior of AI (CsI), non-etching behavior of AM (Cs), and Iodine atoms w.r.t SLG.

Supporting Information

Supporting Information is available from the Wiley Online Library or from the author.

Conflict of Interest

The authors declare no conflict of interest.

Data Availability Statement

The data that support the findings of this study are available from the corresponding author upon reasonable request.

[1] X. Li, X. Yang, J. Zhang, Y. Huang, B. Liu, *ACS Catal.* **2019**, *9*, 2521.

[2] M. H. Rummeli, H. Q. Ta, R. G. Mendes, I. G. Gonzalez-Martinez, L. Zhao, J. Gao, L. Fu, T. Gemming, A. Bachmatiuk, Z. Liu, *Adv. Mater.* **2019**, *31*, 1800715.

[3] S. P. Surwade, S. N. Smirnov, I. V. Vlassiouk, R. R. Unocic, G. M. Veith, S. Dai, S. M. Mahurin, *Nat. Nanotechnol.* **2015**, *10*, 459.

[4] L. Wang, L. W. Drahushuk, L. Cantley, S. P. Koenig, X. Liu, J. Pellegrino, M. S. Strano, J. S. Bunch, *Nat. Nanotechnol.* **2015**, *10*, 785.

[5] A. C. Neto, F. Guinea, N. M. Peres, K. S. Novoselov, A. K. Geim, *Rev. Mod. Phys.* **2009**, *81*, 109.

[6] C. N. R. Rao, A. K. Sood, *Graphene: Synthesis, Properties, and Phenomena*, John Wiley & Sons, Weinheim, Germany **2013**.

[7] Y. Zhu, S. Murali, M. D. Stoller, K. Ganesh, W. Cai, P. J. Ferreira, A. Pirkle, R. M. Wallace, K. A. Cychosz, M. Thommes, *Science* **2011**, *332*, 1537.

[8] D. Branton, D. W. Deamer, A. Marziali, H. Bayley, S. A. Benner, T. Butler, M. Di Ventra, S. Garaj, A. Hibbs, X. Huang, in *Nanoscience and technology: A collection of reviews from Nature Journals* (Ed: P. Rodgers), World Scientific, London **2010**, pp. 261–268.

[9] D. Boukhvalov, M. Katsnelson, *Appl. Phys. Lett.* **2009**, *95*, 023109.

[10] Q. M. Ramasse, R. Zan, U. Bangert, D. W. Boukhvalov, Y.-W. Son, K. S. Novoselov, *ACS Nano* **2012**, *6*, 4063.

[11] W. L. Wang, E. J. Santos, B. Jiang, E. D. Cubuk, C. Ophus, A. Centeno, A. Pesquera, A. Zurutuza, J. Ciston, R. Westervelt, *Nano Lett.* **2014**, *14*, 450.

[12] F. Banhart, J. Kotakoski, A. V. Krasheninnikov, *ACS Nano* **2011**, *5*, 26.

[13] J. C. Meyer, F. Eder, S. Kurasch, V. Skakalova, J. Kotakoski, H. J. Park, S. Roth, A. Chuvilin, S. Eyhusen, G. Benner, *Phys. Rev. Lett.* **2012**, *108*, 196102.

[14] T. Zoberbier, T. W. Chamberlain, J. Biskupek, N. Kuganathan, S. Eyhusen, E. Bichoutskaia, U. Kaiser, A. N. Khlobystov, *J. Am. Chem. Soc.* **2012**, *134*, 3073.

[15] T. Zoberbier, T. W. Chamberlain, J. Biskupek, M. Suyetin, A. G. Majouga, E. Besley, U. Kaiser, A. N. Khlobystov, *Small* **2016**, *12*, 1649.

[16] K. Cao, T. Zoberbier, J. Biskupek, A. Botos, R. L. McSweeney, A. Kurtoglu, A. Markevich, E. Besley, T. W. Chamberlain, U. Kaiser, A. N. Khlobystov, *Nat. Commun.* **2018**, *9*, 3382.

[17] K. T. Chan, J. Neaton, M. L. Cohen, *Phys. Rev. B* **2008**, *77*, 235430.

[18] X. Liu, C. Wang, Y. Yao, W. Lu, M. Hupalo, M. Tringides, K. Ho, *Phys. Rev. B* **2011**, *83*, 235411.

[19] A. Rudenko, F. Keil, M. Katsnelson, A. Lichtenstein, *Phys. Rev. B* **2010**, *82*, 035427.

[20] M. Kühne, F. Börrnert, S. Fecher, M. Ghorbani-Asl, J. Biskupek, D. Samuelis, A. V. Krasheninnikov, U. Kaiser, J. H. Smet, *Nature* **2018**, *564*, 234.

[21] Y. Okamoto, *J. Phys. Chem. C* **2014**, *118*, 16.

[22] J. B. Fenn, M. Mann, C. K. Meng, S. F. Wong, C. M. Whitehouse, *Mass Spectrom. Rev.* **1990**, *9*, 37.

[23] S. Rauschenbach, F. L. Stadler, E. Lunedei, N. Malinowski, S. Koltsov, G. Costantini, K. Kern, *Small* **2006**, *2*, 540.

[24] S. Rauschenbach, R. Vogelgesang, N. Malinowski, J. W. Gerlach, M. Benyoucef, G. Costantini, Z. Deng, N. Thontasen, K. Kern, *ACS Nano* **2009**, *3*, 2901.

[25] S. Rauschenbach, M. Ternes, L. Harnau, K. Kern, *Annu. Rev. Anal. Chem.* **2016**, *9*, 473.

[26] N. Vats, Y. Wang, S. Sen, S. Szilagyi, H. Ochner, S. Abb, M. Burghard, W. Sigle, K. Kern, P. A. van Aken, *ACS Nano* **2020**, *14*, 4626.

[27] S. Y. Davydov, G. Sabirova, *Tech. Phys. Lett.* **2011**, *37*, 515.

[28] E. S. Rittner, *J. Chem. Phys.* **1951**, *19*, 1030.

[29] T. Susi, C. Hofer, G. Argentero, G. T. Leuthner, T. J. Pennycook, C. Mangler, J. C. Meyer, J. Kotakoski, *Nat. Commun.* **2016**, *7*, 13040.

[30] H. Yan, Y. Lin, H. Wu, W. Zhang, Z. Sun, H. Cheng, W. Liu, C. Wang, J. Li, X. Huang, *Nat. Commun.* **2017**, *8*, 1070.

[31] J.-N. Longchamp, C. Escher, H.-W. Fink, *J. Vac. Sci. Technol., B: Nanotechnol. Microelectron.: Mater., Process., Meas., Phenom.* **2013**, *31*, 020605.

[32] P. Giannozzi, S. Baroni, N. Bonini, M. Calandra, R. Car, C. Cavazzoni, D. Ceresoli, G. L. Chiarotti, M. Cococcioni, I. Dabo, *J. Phys.: Condens. Matter* **2009**, *21*, 395502.

[33] P. Giannozzi, O. Andreussi, T. Brumme, O. Bunau, M. B. Nardelli, M. Calandra, R. Car, C. Cavazzoni, D. Ceresoli, M. Cococcioni, *J. Phys.: Condens. Matter* **2017**, *29*, 465901.

[34] P. Giannozzi, O. Baseggio, P. Bonfà, D. Brunato, R. Car, I. Carnimeo, C. Cavazzoni, S. De Gironcoli, P. Delugas, F. F. Ruffino, *J. Chem. Phys.* **2020**, *152*, 154105.

[35] H. J. Monkhorst, J. D. Pack, *Phys. Rev. B* **1976**, *13*, 5188.

[36] K. Momma, F. Izumi, *J. Appl. Crystallogr.* **2008**, *41*, 653.

[37] G. Kresse, J. Furthmüller, *Phys. Rev. B* **1996**, *54*, 11169.

[38] G. Kresse, D. Joubert, *Phys. Rev. B* **1999**, *59*, 1758.